communications earth & environment

Article

A Nature Portfolio journal

https://doi.org/10.1038/s43247-025-02479-8

Substantial continental temperature rise over the Paleocene-Eocene Thermal Maximum in the Pyrenees

Gábor Újvári[1,2] ✉, Sándor Kele[1,2], László Rinyu[3], Aitor Payros[4], Kim H. Stadelmaier[5], János Kovács[6,7], Ivett Kovács[1,2], Bernadett Bajnóczi[1,2], Victoriano Pujalte[4], Birger Schmitz[8] & Stefano M. Bernasconi[9]

The Eocene period experienced several hyperthermal events with the Paleocene-Eocene Thermal Maximum being the most significant. During this event, global mean surface temperatures were 5–6 °C higher and latitudinal temperature gradients were reduced compared to the late Paleocene. Unlike marine temperature records, terrestrial archives are limited, posing challenges for testing climate model competence in simulating the magnitude and spatial patterns of temperature change under a high carbon dioxide climate. Here we analysed mudstone paleosols from the Tremp Group in Spain to reconstruct soil temperatures using carbonate nodules. Clumped isotopes revealed median calcification temperatures of 33.9 and 39.2 °C for the Late Paleocene and Paleocene-Eocene Thermal Maximum, respectively. The findings suggest a ~5 °C summer soil temperature increase during the Paleocene-Eocene Thermal Maximum. Continental proxy and model data indicate reduced (0.7–0.4 °C/degree) meridional temperature gradients between 25 and 75°N latitudes, indicating more uniform heat distribution across latitudes than at present.

Superimposed on the generally warm late Paleocene (LP) climate, the Paleocene-Eocene Thermal Maximum (PETM, ~56 Ma) was a 170–200 thousand year (kyr) long hyperthermal event[1,2], when deep ocean and sea surface temperatures (SSTs) were globally 4–5 °C warmer than over the LP[3–5]. Although the PETM onset occurred near a 405-kyr eccentricity maximum, suggesting an orbital trigger[2,6], it is most likely to be driven by geologically rapid (3–5 kyr)[7] addition(s) of large amounts (~3000–10,000 Pg C) of ^{13}C-depleted CO_2 to the carbon reservoirs of the Earth surface[7–10], most probably originating from volcanism associated with the North Atlantic Igneous Province[11–14]. Both proxy and model evidence document a substantial alteration of the hydrological cycle[15–17] and intensified chemical weathering[18,19] associated with global warming over the PETM.

Not only SSTs[20], but also the much sparsely available continental temperature proxy data indicate reduced latitudinal thermal gradients[21–23] and warm continental interiors[24,25] under the early Eocene greenhouse climate. However, the locations where climate change over the Paleocene–Eocene (P–E) boundary is reliably resolved using quantitative proxy data are limited and are unevenly distributed in space[26]. The relatively sparse proxy network hinders the derivation of the spatial patterns of temperature changes across the PETM and proxy-model data comparison. To fill one of these gaps, we provide temperature estimates using the clumped isotope composition (Δ_{47}) of soil carbonates (SCs) collected in the Esplugafreda sedimentary record, Spain, a well-known and investigated subtropical (paleolatitude ~32.3°N; Fig. 1 and Supplementary Fig. 1) continental record of climate and hydrological cycle changes across the P–E boundary[15,27–30]. The upper Maastrichtian to lower Ypresian terrestrial deposits of the Tremp Group at Esplugafreda is made up of ~250 m of red/grey/yellow mudstones with abundant paleosols, deposited in a coastal alluvial setting[15,27,31]. The paleosols, which are dominantly cumulative in nature[32], contain widespread centimetre-sized, pedogenic soil nodules and gypsum indicating a semi-arid to arid paleoenvironment with seasonal precipitation[15]. The P–E boundary is located near the top of the continental

[1]Institute for Geological and Geochemical Research, HUN-REN Research Centre for Astronomy and Earth Sciences, Budapest, Hungary. [2]CSFK, MTA Centre of Excellence, Budapest, Hungary. [3]Isotope Climatology and Environmental Research Centre, HUN-REN Institute for Nuclear Research (ATOMKI), Debrecen, Hungary. [4]Department of Geology, Faculty of Science and Technology, University of the Basque Country UPV/EHU, Bilbao, Spain. [5]Institute of Meteorology and Climate Research, Troposphere Research (IMKTRO), Karlsruhe Institute of Technology (KIT), Karlsruhe, Germany. [6]Department of Geology and Meteorology, University of Pécs, Pécs, Hungary. [7]Environmental Analytical and Geoanalytical Research Group, Szentágothai Research Centre, University of Pécs, Pécs, Hungary. [8]Department of Physics, University of Lund, Lund, Sweden. [9]Department of Earth Sciences, ETH Zürich, Zürich, Switzerland.
✉e-mail: ujvari.gabor@csfk.hun-ren.hu

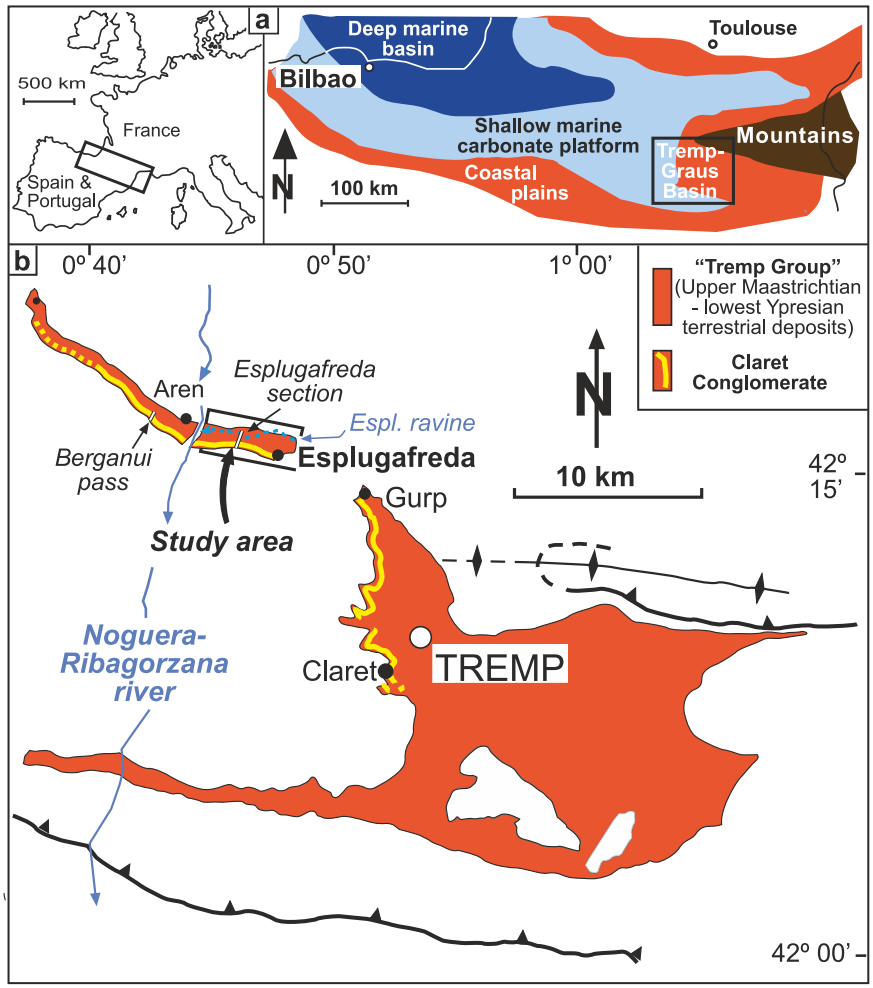

Fig. 1 | Location of the Esplugafreda section in the Tremp-Graus Basin. a Simplified early Paleogene palaeogeography of the Pyrenean domain (modified from Pujalte et al.[28]). **b** Outcrop map of the Tremp-Graus Basin in the Esplugafreda and Claret sectors, with the location of reference sections (from Payros et al.[30]).

section (Fig. 2), based on a pronounced negative carbon isotope excursion (CIE) found in soil carbonates[15,33]. The CIE spans more than 15–20 m of yellow cumulate paleosols formed during the PETM (Supplementary Figs. 2–4). The post-PETM interval in the Esplugafreda section comprises 20 m of red paleosols rich in gypsum and characterised by normal soil nodule $\delta^{13}C$ values[15,28,30].

Alluvial deposits of the Esplugafreda section were formed in a climatically sensitive region at the northernmost part of the subtropical zone, a latitudinal belt fringing the temperate climate zone. Indeed, vertisols of the Esplugafreda Formation (EF) attest climatic regime shifts from Mediterranean to subtropical monsoon climate over the LP[31] and even more profound climate change from temperate, humid subtropical climate with hot summers (Köppen-Geiger climate class: Cfa) to tropical climate across the P–E boundary[34]. Climatic swings of this magnitude must have been preserved in soil carbonates, which provide the only means of quantitatively reconstructing temperature changes and precipitation $\delta^{18}O$ values for this key site over the LP and PETM. Carbonate clumped isotope thermometry[35,36] allows paleotemperature reconstructions without requiring independent estimates of the oxygen isotope composition of soil water (i.e. precipitation) from which the carbonate grew. Pedogenic carbonates are assumed to form in isotopic equilibrium with soil CO_2 and water[37]. Local environmental and soil conditions, including soil temperature (T_{soil}), moisture and pCO_2[38], are the major controls on the stable carbon and oxygen isotopic compositions of soil carbonate ($\delta^{13}C_{carb}$, $\delta^{18}O_{carb}$), which provide a time-integrated record of these parameters over hundreds to thousands of years of carbonate formation. While vegetation, soil productivity/CO_2 and soil temperature and water isotopic compositions define $\delta^{13}C_{carb}$ and $\delta^{18}O_{carb}$[37,39], T_{soil} is the only factor that determines clumped isotope compositions of soil carbonates ($\Delta_{47\text{-carb}}$)[40,41]. Soil carbonate formation usually follows frequent dewatering and CO_2 outgassing events during warm/dry episodes of the summer season[38], causing a warm season bias in carbonate growth and thus SC-derived clumped isotope temperatures ($T_{\Delta47\text{-carb}}$)[40–44]. A warm-season biased carbonate formation is likely valid for the mudstone paleosols (vertisols) of the Esplugafreda sedimentary record, as soil pCO_2 is dominantly controlled by cracking and shrink-swell processes in vertisols, occurring during late spring and summer[45]. In summary, $\Delta_{47\text{-carb}}$ is a promising proxy for quantifying the magnitude of warming recorded in continental sediments at Esplugafreda over the LP and PETM and understanding the climatic response of the former subtropical Pyrenean region to high CO_2 conditions. Furthermore, the $T_{\Delta47\text{-carb}}$ proxy data can be useful to assess model competence of the Deep Time Model Intercomparison Project (DeepMIP)[46] and contribute to paleoclimate data assimilation to improve estimates of the magnitude and spatial patterns of climatic changes during the PETM[26].

We find that the mudstone paleosols of the Esplugafreda record contained carbonate nodules with internal features suggesting near-surface precipitation and high Mn^{2+} content, indicating reducing conditions potentially related to temporary aquic soil conditions. The PETM was marked by clear CIEs of ~–2.0‰ in organic matter and –5.5‰ in soil carbonates. Clumped isotope analyses of these nodules revealed calcification temperatures being in interquartile ranges of 27.5–37.1 °C for the LP and 35.3–41.2 °C for the PETM. Calculated median soil temperatures were 33.9 °C and 39.2 °C for the LP and PETM intervals, respectively, suggesting a significant soil warming of ~5 °C during the PETM when excluding potential seasonal effects on carbonate formation.

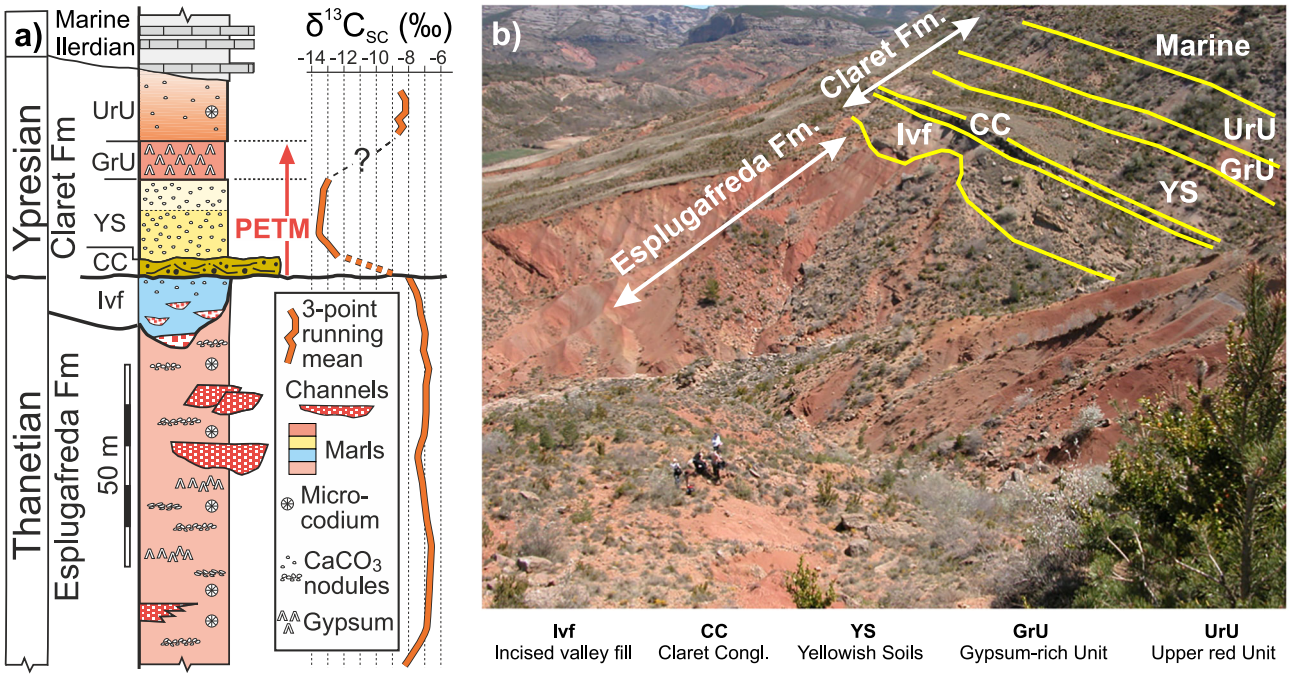

Fig. 2 | Stratigraphy of the Esplugafreda sedimentary record. a Synthetic lithostratigraphy and soil carbonate $\delta^{13}C$ isotope profile of the Paleocene–Eocene interval (after Payros et al.[30], modified from Pujalte et al.[28]) with (**b**) a field photo of the Esplugafreda and Claret Formation members in the western part of the Esplugafreda sector (from Pujalte et al.[28]).

Results

Sediment grain size, mineralogy and organic matter $\delta^{13}C$

The grain size distributions (GSDs) of the Esplugafreda sediments are relatively uniform throughout the record (Supplementary Fig. 5). In general, GSDs are uni- to polymodal, dominantly fine skewed with the mode/mean in the coarse silt/very fine sand fraction (Fig. 3). The sediments are poorly sorted and belong to the sandy mud/muddy sand textural groups and sandy silt/silty sand category (Supplementary Fig. 6). Mudstone paleosols of the EF between 140 and 110 m composite depth were found to be much finer (mean grain size (MGS): 15–35 µm) than the overlying deposits, which exhibit significant internal variations in MGS between 20 and 80 µm without clear grain size trends (Fig. 3).

The clay mineral assemblage of the upper Paleocene sediments is dominated by illite and smectite (45 ± 7, 40 ± 7 wt%) with smaller amounts of kaolinite and chlorite (7 ± 2, 8 ± 1 wt%, Supplementary Dataset 1). Clay mineralogy of the incised valley fill resembles that of upper Paleocene mudstone paleosols (Supplementary Fig. 7). By contrast, the PETM yellowish soils are lower in illite (31 ± 6 wt%) but have more smectite and kaolinite (48 ± 6, 12 ± 2 wt%), which is also reflected in elevated kaolinite/illite (klt/ilt) and smectite/(illite + chlorite) (sme/(ilt + chl)) ratios (Fig. 3 and Supplementary Dataset 1). The Upper reddish Unit sediments show relatively smectite-poor compositions with higher illite contents (65–66 wt%).

Organic matter $\delta^{13}C$ of the EF mudstone paleosols of LP age vary around a median (Q_2) value of –25.19 ‰ and exhibit a weak negative trend towards the younger sediments (Fig. 3). The incised valley fill deposits generally show more positive $\delta^{13}C_{org}$ values compared to the underlying EF paleosols (median: –24.86‰), with a negative excursion exceeding 1‰. The PETM yellowish soils provide the most negative $\delta^{13}C_{org}$ values in the entire record, sometimes lower than –27‰, fluctuating around a median value of –26.83‰. The calculated CIE_{org1} and CIE_{org2} values, which are based on the difference between the median $\delta^{13}C_{org}$ values of incised valley fill (Ivf), LP and PETM sediments, are –1.97‰ and –1.64‰, clearly identifying the body of PETM. Paleosols of the Gypsum-rich Unit and Upper reddish Unit display heavier carbon isotope compositions again.

Soil carbonate petrography

In general, soil carbonates originating from LP paleosols of the EF are slightly larger (1–2 cm) in size than those of the PETM yellowish soils (0.5–1 cm, Supplementary Fig. 8a). All investigated SCs exhibit features of the alpha-type end-member[47], dominantly consisting of dense, continuous, non-porous micritic groundmass incorporating clay to silt-sized (Supplementary Fig. 8b, d) or rarely sand-sized (Supplementary Fig. 8e) floating framework grains. Some SCs include zones of displacive/replacive spars and microspars potentially resulting from dissolution/recrystallisation of some micrite (e.g. Supplementary Fig. 8d). Few SCs comprise coalesced larger calcite crystals cemented by sparry calcite (Supplementary Fig. 8c). Cracking features are absent. CL images of most SCs show bright, relatively homogeneous orange to reddish cathodoluminescence of calcite groundmass (Supplementary Fig. 8b, d, e), sometimes with less bright or even dull luminescence when calcites are coarser-grained (Supplementary Fig. 8c). This latter form very rarely occurs and only in EF paleosols.

Soil carbonate stable carbon, oxygen and clumped isotope compositions

Following a thorough review of our measurement datasets, a single sample (ITS/W-YS7, 8-16 July 2022) was selected for which isobaric contamination could not be excluded. Consequently, the results of this carbonate subsample were not considered further. Soil carbonates of the EF yield $\delta^{13}C_{carb}$ values between –8.55 and –5.85 ‰, while the PETM yellowish soil carbonates are significantly more negative (–13.84 to –10.12 ‰). The CIE_{carb} value, calculated as the difference between the median $\delta^{13}C_{carb}$ values of LP (EF, –6.93 ‰) and PETM carbonates (YS, –12.44 ‰), is –5.51 ‰ (Fig. 4a). A much smaller, –1.40 ‰ difference can be observed in the oxygen isotope compositions of these two SC populations ($\delta^{18}O_{carb}$: –5.54 to –4.13 in LP versus –6.15 to –5.81 ‰ in YS; Fig. 4), which almost disappears when SC-derived soil water $\delta^{18}O$ values are considered (Fig. 4b).

The statistical analysis of Δ_{47}-based paleotemperatures ($T_{\Delta47\text{-}carb}$) provide a median soil carbonate formation of 33.9 °C with an interquartile (Q_1-Q_3) range of 27.5–37.1 °C during the LP (Fig. 4c, d), considering all $\Delta_{47\text{-}carb}$ measurements of EF carbonates. By contrast, much higher temperatures

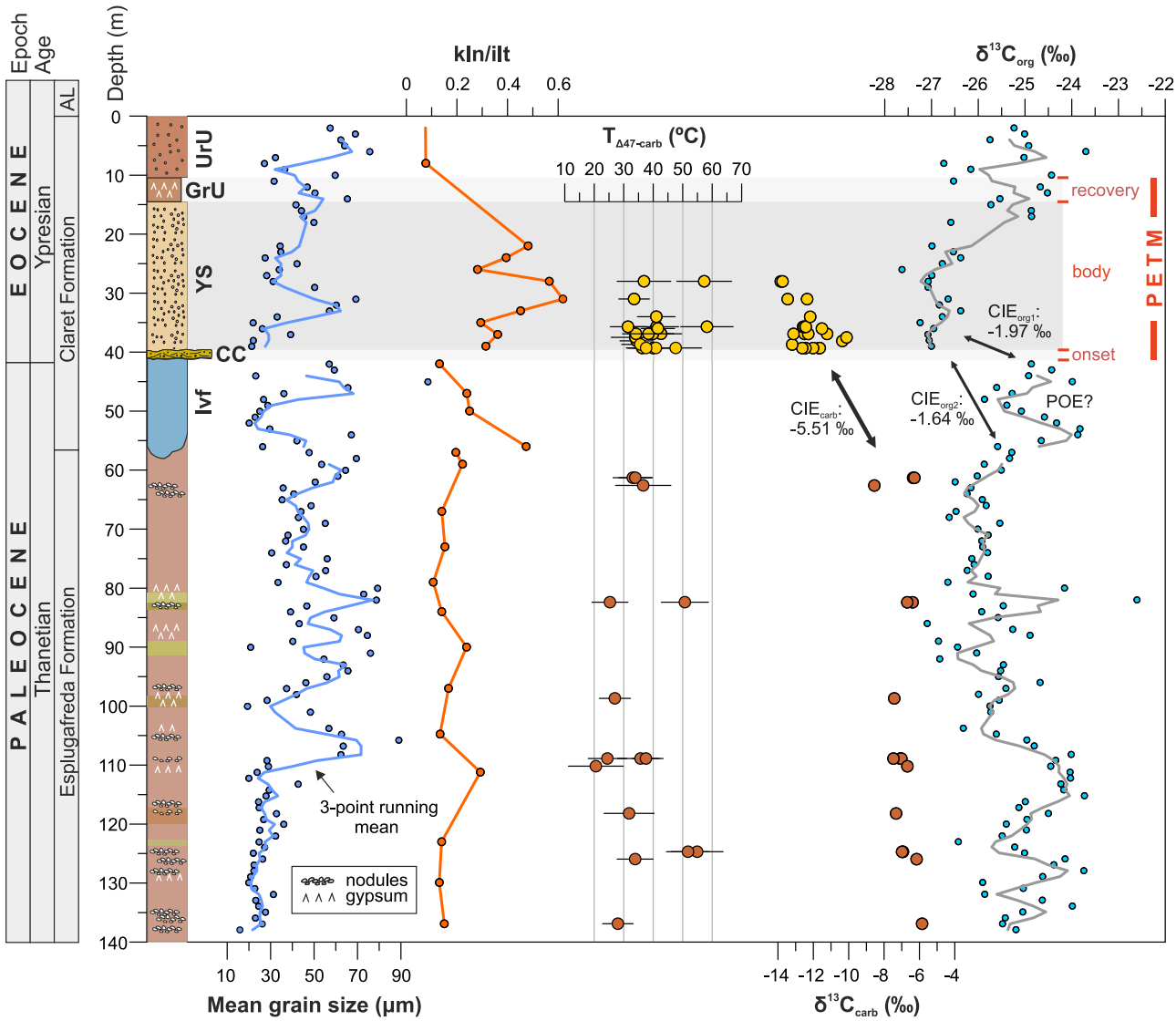

Fig. 3 | Grain size, clay mineralogy, soil carbonate and organic matter $\delta^{13}C$ compositions and soil carbonate formation temperatures of the composite Esplugafreda record as a function of depth. AL alveolina limestone, Ivf incised valley fill, CC claret conglomerate, YS yellowish soils, GrU gypsum-rich unit, UrU upper red unit; kln kaolinite, ilt illite, POE pre-onset excursion, CIE carbon isotope excursion based on $\delta^{13}C_{carb}$ and $\delta^{13}C_{org}$. CIE_{org1-2} and CIE_{carb} are defined in the text. Error bars of soil carbonate calcification temperatures represent 95% CL.

were recorded by soil carbonates of the PETM yellowish soils (median: 39.2 °C), with a much higher interquartile range (35.3–41.2 °C) than over the LP. As demonstrated by a two-sided Wilcoxon ranksum and Kruskal-Wallis test (Supplementary Table S1), the calculated medians are different, and the $T_{\Delta47\text{-carb}}$ values of LP and PETM carbonates do not originate from the same distribution at the 95% confidence level. Both the difference in the median values (5.3 °C) and the positive shift in the interquartile range provide evidence for significant warming of soils over the PETM.

Paleoclimate simulation results

Near-surface air temperatures derived for the paleo-location of the Esplugafreda site using eight Earth system models of the DeepMIP for 280–1680 ppm atmospheric CO_2 concentrations demonstrate increasing monthly temperatures, with mean annual and summer season air temperatures (MAT, T_{JJA}) between 19.6 and 29.6 (280–1120 ppm), as well as 26.8–38.4 °C (280–1120 ppm) (Fig. 5a and Supplementary Fig. 9). Model results indicate seasonal variations in temperature rise, with the winter season warming being more intense than for the summer season (Supplementary Fig. 10). Simulated precipitation rates do not vary much between 280 and 840 ppm CO_2 levels (mean annual precipitation/MAP: 905–972 mm) with the highest rates/values over the summer and early autumn (Fig. 5b and Supplementary Fig. 11). Ensemble means of the simulations run for more extreme PETM-like CO_2 concentrations provided smaller (1120 ppm) and much higher (1680 ppm) precipitation rates and MAP (585 and 1372 mm), especially for June to October (Fig. 5b and Supplementary Fig. 10).

The DeepMIP models demonstrate that the meridional temperature distribution also changes significantly with increasing CO_2 concentration (Fig. 6), particularly in the extratropical region. The simulation results are otherwise in relatively good agreement with the continental proxy data for the LP (2–3 × CO_2) and PETM (4–6 × CO_2), particularly in regions <50°N latitude. Proxy data from higher latitudes (50–77°N) suggest that continental warming modelled at the highest CO_2 levels underestimates values that were characteristic at the Paleocene-Eocene boundary, although the sparseness of the proxy data makes this observation uncertain. At low CO_2 levels (1× CO_2), the meridional (latitudinal) temperature gradient (Fig. 6a) is around the present-day value of 0.8–1.0 °C/deg. between 25 and 75°N latitudes. However, at higher CO_2 concentrations, the thermal gradient

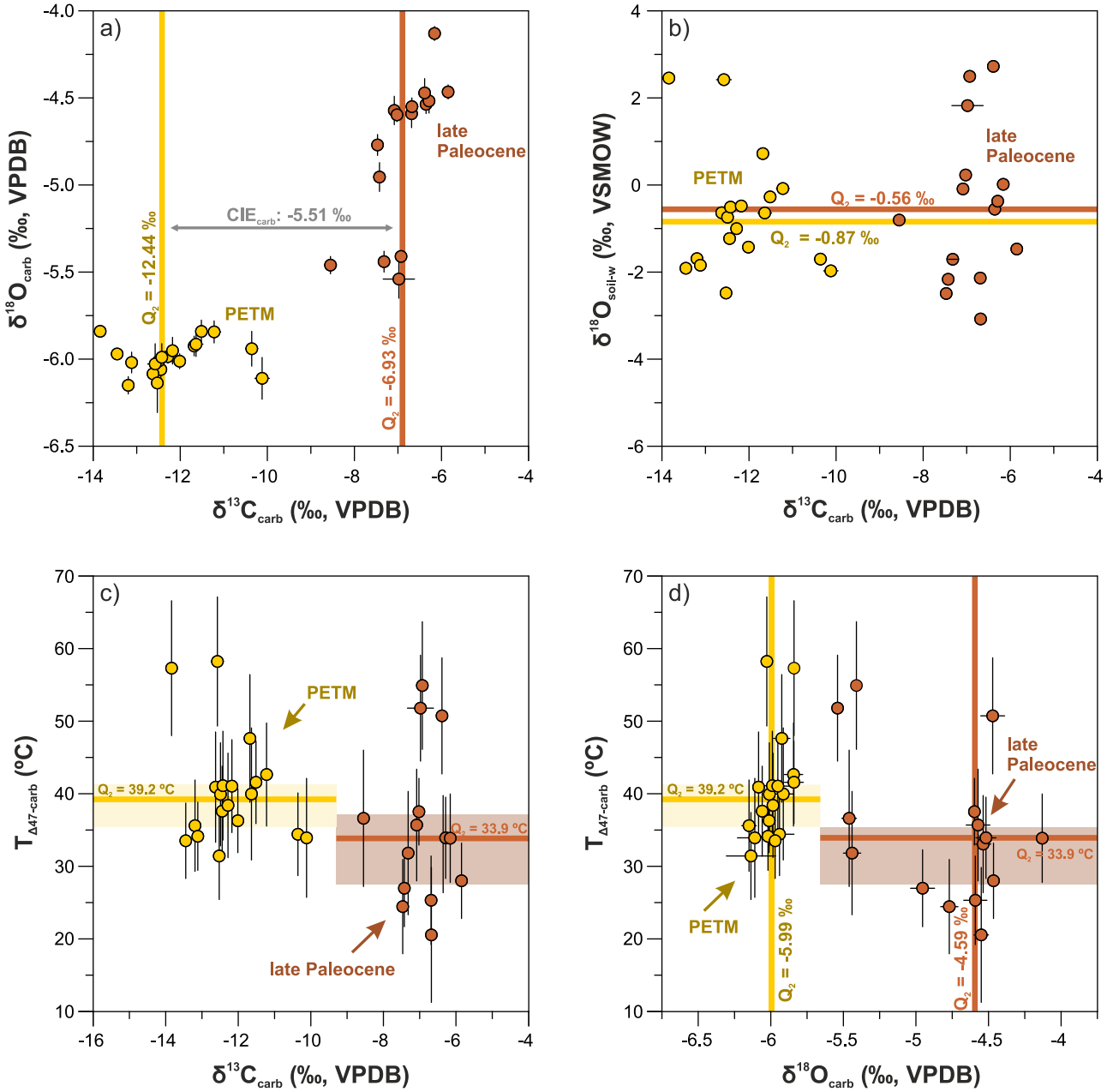

Fig. 4 | Stable isotope compositions and formation temperatures of soil carbonates of late Paleocene and early Eocene (PETM body) age from the Esplugafreda record. a, **b** Carbon and oxygen isotope compositions and **c**, **d** clumped isotope temperatures. See Table 1 for stable isotope data and sample information. Note that error bars are in many cases smaller than symbols. Q_2 denotes the median values, and the carbon isotope excursion (CIE) in (**a**) is based on the difference of median $\delta^{13}C_{carb}$ values of LP and PETM carbonates. Soil water $\delta^{18}O$ data displayed on (**b**) were calculated from $\delta^{18}O_{carb}$ and $T_{\Delta47\text{-}carb}$ values as defined in Table 1. In (**c**, **d**) the colour shadings represent the interquartile range (Q_1–Q_3) of the soil carbonate temperatures ($T_{\Delta47\text{-}carb}$), with the median value (Q_2) indicated. Error bars of soil carbonate calcification temperatures represent 95% CI. More information is provided in the text.

declines to ~0.6–0.7 °C/deg. between 25 and 50°N, and even to 0.4 °C/deg. between 50 and 75°N.

Discussion

Sedimentary environment and soil carbonate formation in the Esplugafreda record

Terrestrial deposits of the Esplugafreda and Claret Formations record sedimentation in changing alluvial environments under a generally arid/semi-arid climate during the LP and early Eocene[28–30]. Two successive pedotypes were described in mudstone paleosols (basically vertisols) of the EF representing Mediterranean climate with arid soil conditions (Pont d'Orrit pedotype) followed by monsoon climate with aquic soil conditions (Areny pedotype)[31]. Over the PETM, formation of the Claret Conglomerate demonstrates a substantially enhanced hydrological cycle and high kaolinite influx implies higher continental physical erosion rates[15,27]. Our grain size data indicate that the LP and PETM paleosols are basically very similar in terms of soil textures, but the Pont d'Orrit pedotype is characterised by finer grain size at the base (140–110 m) of the EF. Whether this relates to the different climate regime (Mediterranean, Pont d'Orrit pedotype) and/or the alluvial environment in which these soils formed is unclear. The significantly increased klt/ilt and sme/(ilt + chl) ratios in the PETM yellowish soils (Fig. 3 and Supplementary Dataset 1) further confirm observations of Schmitz and Pujalte[27], and in line with their interpretation, it is most probably attributable to higher

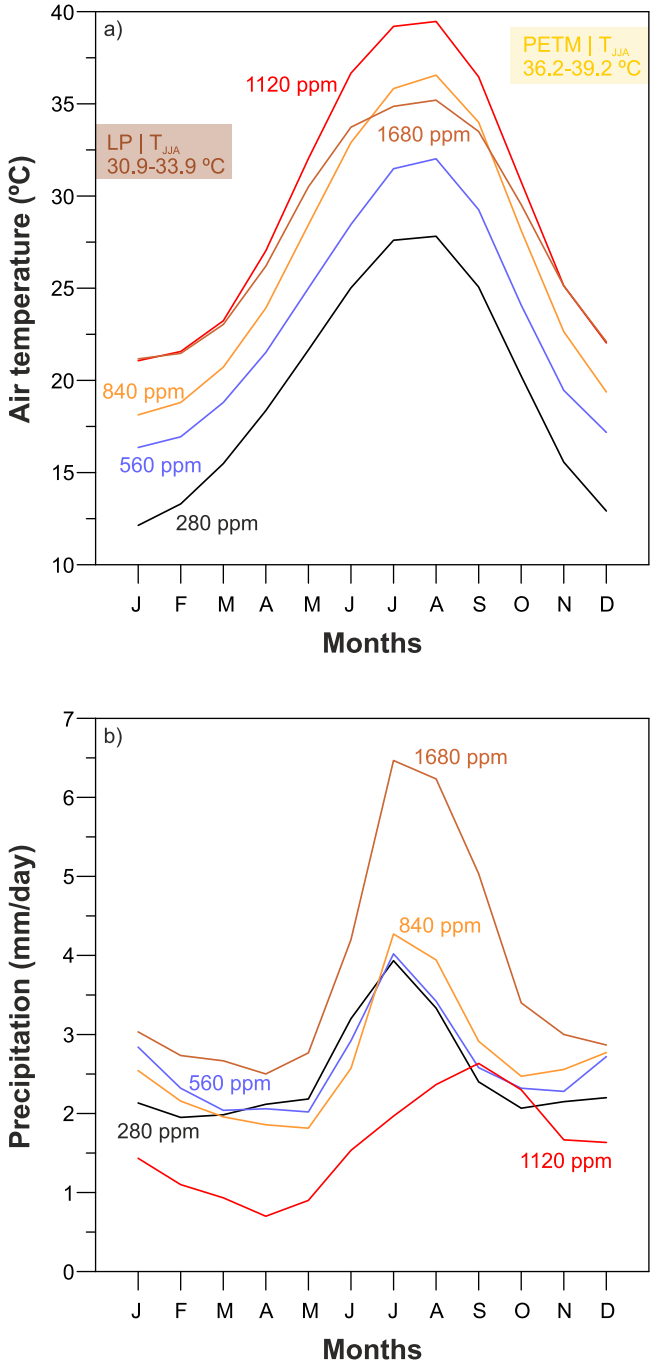

Fig. 5 | Simulated meteorological parameters for the paleo-location of the Esplugafreda sedimentary record for various atmospheric CO_2 concentrations. **a** near-surface air temperature and (**b**) daily precipitation. Model data displayed are ensemble means of eight Earth system models of DeepMIP[45]. Reconstructed (soil carbonate-based) T_{JJA} values for the LP and PETM are also shown for comparison.

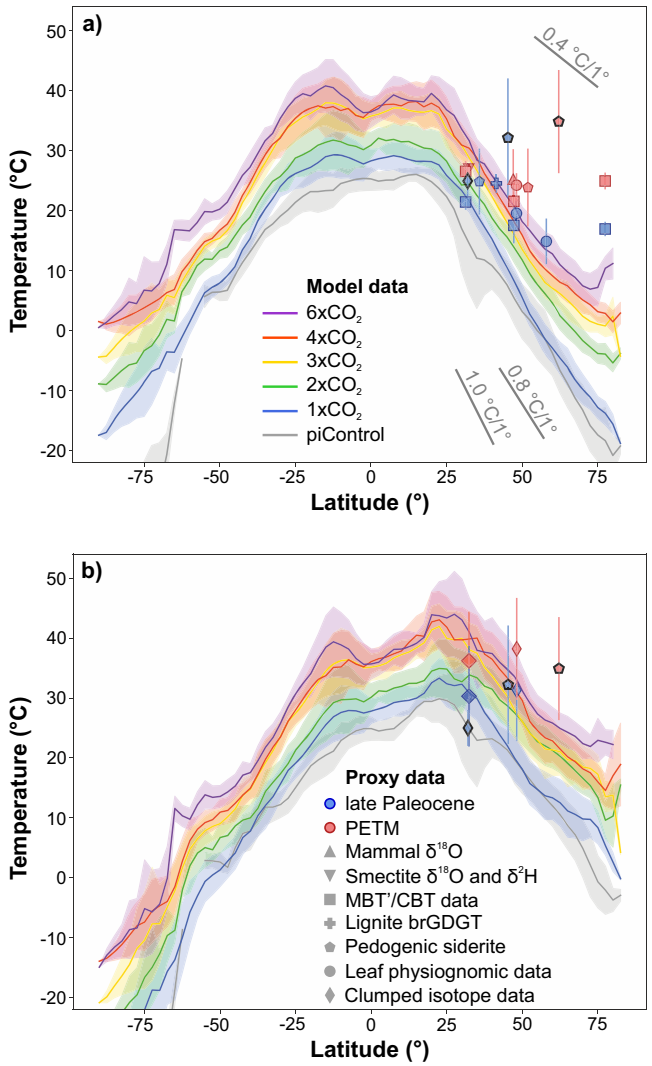

Fig. 6 | Simulated and proxy-based continental temperatures over the Late Paleocene and PETM. **a** Mean annual temperatures (MAT) and (**b**) summer mean temperatures (T_{JJA}) as a function of latitude. Modelled temperatures are from DeepMIP simulations and represent the ensemble means (lines) with one standard deviation (shaded areas). Proxy-based temperatures are from the literature (see Supplementary Dataset 2) and this study. Error bars of proxy temperature data represent 2 sigma uncertainties. Proxy symbols with bold frames denote summer-biased MAT.

detrital input of kaolinite and smectite from deeper physical erosion of rocks in the hinterland.

The form and size of collected soil nodules (Supplementary Fig. 8) and the presence of a suite of carbonate textures such as floating silicate grains and micrite-microspar fabrics implies that the studied carbonates originated from near-surface precipitation[48]. However, carbonate nodules in mudstones may be pedogenic or the result of shallow groundwater invasion of the vadose zone, and little or no difference exists in their petrographic character[49]. The mostly bright, orange to reddish cathodoluminescence of calcite groundmass (Supplementary Fig. 8) of the studied carbonates is indicative of elevated Mn^{2+} concentrations[50] and precipitation under low-Eh (i.e. reducing) conditions[51]. These observations imply that the investigated nodules may have dominantly formed in stagnant water under temporary aquic conditions, in agreement with the abundant redoximorphic features in EF vertisols[31] and frequent purple mottling of the yellowish soils (Supplementary Fig. 4c–e), demonstrating imperfectly or poorly drained paleosol conditions[52] for most of the year. As such, soil carbonates may have formed during warmer, drier periods when soil pCO_2 was reduced. In this process, stagnant soil water became supersaturated in Ca ions, leading to carbonate precipitation under water-logged conditions. However, it is also conceivable that stagnant water may have potentially disappeared completely from the soil for shorter periods. In vertisols, soil CO_2 (and soil moisture) is controlled by soil crack porosity and ultimately by shrink-swell processes, which are amplified during dry periods (typically late spring to summer)[45]. For these reasons, it seems very likely that although soil carbonate Δ_{47} values in fine-grained soils often reflect MAT[53,54], in vertisols, shrink-swell phenomena (and cracking) are the

primary drivers of pedogenic carbonate precipitation. Consequently, the $T_{\Delta47\text{-carb}}$ values are most likely warm-season biased temperatures.

CIE recorded in organic matter and soil carbonates

Estimates of the PETM carbon cycle perturbation rely on the magnitude of CIE associated with this hyperthermal event[1]. However, there is a discrepancy between CIE values preserved in marine sediment organic matter (2–5‰)[1] and continental soils (3–7‰)[55]. Likewise, terrestrial organic matter and soil carbonates record systematic differences in CIE magnitudes[56]. In our $\delta^{13}C_{org}$ dataset, both the LP and PETM sediment carbon isotope values are slightly more negative than those measured by Manners et al.[55] for the Esplugafreda record, but the calculated CIE_{org1} (−1.97‰, Fig. 3) is in good correspondence with the previously established CIE magnitude of ~2‰. This provides further evidence that the yellowish soils represent the body of PETM. More positive values around −25‰ of the Gypsum-rich Unit potentially mark the recovery phase of the PETM[28,30]. A striking feature of the $\delta^{13}C_{org}$ record is the more positive values of incised valley fill sediments compared to the EF paleosols and the ~1.5‰ negative shift within the Ivf deposits. The so-called pre-onset excursion (POE), which marks the first massive carbon release right before the PETM[10], was identified in Ivf carbonates[33]. Considered in isolation, the negative $\delta^{13}C_{org}$ excursion in Ivf sediments resembles the POE. However, even the most negative values of this potential POE are not more negative than most of the $\delta^{13}C_{org}$ of EF paleosols (Fig. 3). Thus, in contrast to $\delta^{13}C_{carb}$ of Tremblin et al.[33], our $\delta^{13}C_{org}$ dataset does not provide unambiguous evidence for the appearance and preservation of the POE in the Esplugafreda record. Unfortunately, soil carbonates were not found in and analysed from the Ivf sediments.

Compared to the organic matter $\delta^{13}C$ record, the $\delta^{13}C_{carb}$ values obtained from SCs yield a more than 2 times larger average CIE_{carb} (−5.51 ‰, Fig. 4a), although this value was calculated from SCs collected in the mudstone paleosols of the EF (LP) and yellowish soils (PETM) and did not include carbonates from Ivf sediments. This is surprisingly consistent with a CIE_{carb} of −5.7 ‰ recorded in paleosol carbonates at Polecat Bench, Bighorn Basin, Wyoming[10]. The 3.9‰ difference in CIE_{org2} and CIE_{carb} in our records exceeds that (~2‰) preserved in organic matter and soil nodules in paleosols of the Bighorn Basin[56]. The discrepancy between CIE values based on $\delta^{13}C_{org}$ and $\delta^{13}C_{carb}$ in the interpretation of Gallagher et al.[56] is most probably caused by increased soil respiration rates and/or a seasonal shift in carbonate formation and less likely by soil methane oxidation.

Soil water $\delta^{18}O$ and temperature reconstructions for the LP/PETM

Measured soil nodule $\delta^{18}O_{carb}$ values indicate a relatively small, 1.4‰ negative shift (calculated from the medians) in SCs formed over the PETM compared to LP nodules (Fig. 4a, d). This is, however, an effect of calcification temperatures, as the calculated $\delta^{18}O_{soil\text{-}w}$ values representing local precipitation $\delta^{18}O$ only reflect minor changes (median offset: −0.31‰) in the source water oxygen isotope compositions (Fig. 4b). Absolute $\delta^{18}O_{soil\text{-}w}$ values dominantly vary within the range of ~−3 to +3‰ for both SC populations of LP and PETM age. The limited shift in precipitation $\delta^{18}O$ across the P–E boundary is basically very similar to modelled surface ocean $\Delta\delta^{18}O$ (−0.5 to −1 ‰) around the Iberian Peninsula over the LP to PETM[57] and may indicate that precipitation sources did not change much in this interval.

SC calcification temperatures ($T_{\Delta47\text{-carb}}$) for both intervals (LP and PETM) were found to be in a broad range between 20.5 ± 9.3 and 58.2 ± 8.9 °C (error: 95% CL), with interquartile ranges of LP and PETM carbonates within 27.5–37.1 and 35.3–41.2 °C (Fig. 4c). While some SCs were found to be relatively homogeneous in terms of recorded formation temperatures (e.g. ITS-EF sc 5.3 or ITS/E-YS9, Table 1), others were heterogeneous with significant internal variations in $T_{\Delta47\text{-carb}}$ exceeding 10–15 °C (e.g. ITS-EF sc 19.9, ITS/E-YS13). Repeat measurements on SCs yielding very low or high $T_{\Delta47\text{-carb}}$ values (e.g. ITS/W-YS10, ITS/E-YS13 or ITS-EF sc 26.40) usually gave calcification temperatures close to or within the interquartile range of $T_{\Delta47\text{-carb}}$ values characteristic for the central groups of carbonates. The effect of (1) isobaric contaminants and (2) kinetic fractionation are among the potential reasons for the sometimes large internal variations of $T_{\Delta47\text{-carb}}$. Geological reasons may include (3) reprecipitation of micritic carbonate during shallow burial and subsequent exhumation of Esplugafreda sediments, (4) carbonate growth at changing depths in the paleosols over hundreds to thousands of years of nodule formation, and (5) a seasonal shift in SC growth.

It is well-known that N_2O, hydrocarbons, chlorinated hydrocarbons and sulphur-bearing contaminants may cause isobaric interference during Δ_{47} analyses of CO_2[58–60]. A recent study demonstrated that nitrate-derived NO_2 constitutes an isobaric interferent for the extracted CO_2 for some carbonates, which cannot be effectively removed during gas purification and may cause $-\Delta_{47}/+\Delta_{48}$ bias, leading to an overestimation of formation temperatures[61]. In our soil carbonate clumped isotope dataset, no clear relationship was found between Δ_{48} WG (PBL) and calcification temperatures (Supplementary Fig. 12 and Supplementary Datasets 3-4). This observation implies that a robust correlation between the measured elevated Δ_{48} WG (PBL) values and possible nitrate contamination of the studied carbonate samples cannot be demonstrated with the analytical system employed. Since Fiebig et al.[61] found that the ETH-3 standard is affected by nitrate contamination a bleaching experiment was performed in October 2024 using 1 ml 2.5% NaOCl on 30 mg ETH-3 samples with a reaction time of 8 h. Altogether, 20 replicates of bleached ETH-3 were measured, using non-bleached ETH-3 (along with ETH-1 and ETH-2) as standard during the data processing. As shown in Supplementary Table 2, the Δ_{47} values of bleached (0.618 ± 0.013‰) and non-bleached (0.613 ± 0.006‰) ETH-3 statistically overlap with the reference Δ_{47} value of ETH-3 (0.6132‰). Considering these findings, the elevated temperatures obtained for some carbonates are unlikely to be the result of nitrate contamination or at least this cannot be detected using our measurement system. Consequently, no objective criteria were found to exclude these values from the interpretations.

Regarding explanation (2) CO_2 degassing via bicarbonate dehydration, which is the dominant reaction at typical soil pH levels during carbonate precipitation, may often result in disequilibrium isotope signatures with ^{13}C and ^{18}O enrichment and lower Δ_{47} values in calcite relative to the expected equilibrium isotope composition[44,62,63]. Guo[64] developed a model of kinetic isotope fractionations associated with bicarbonate dehydration. This model predicts that, at 25 °C, for every 1‰ increase in calcite $\delta^{18}O$, there is a corresponding 3.26‰ increase in $\delta^{13}C$ and a ~0.022‰ decrease in Δ_{47}. Given the findings of Guo[64] the sometimes substantial (>10 °C) temperature variations measured in certain soil carbonates are predicted to result in several permil shifts in $\delta^{13}C$ and $\delta^{18}O$ within a single carbonate. By contrast, soil carbonates were found to be very homogeneous in terms of carbon and oxygen isotope compositions (Table 1). Furthermore, an anomalous increase in calcification temperatures (lower Δ_{47}) due to kinetic fractionation would be expected to be associated with higher $\delta^{13}C$ and $\delta^{18}O$ values for these sub-samples. However, such a positive relationship appears not to be evident in the data shown in Fig. 4c, d. Thus, while kinetic effects cannot be ruled out entirely for the unusually high calcification temperatures, they do not appear to be significant for these subsamples.

As for explanation (3), several SCs incorporate zones of sparry calcite, and while we focussed on micro-sampling micritic carbonate, potentially unintentionally sampled fractions of sparry calcite invisible at that scale. Regarding explanation (4), it may have a limited effect on SC temperatures as the development of cumulate soils is associated with low sedimentation rates (0.05–0.5 mm/yr)[31,32]. Therefore, considering continuous aggradation and zero surface erosion of soils, a growing nodule gets to a deeper position in the soil profile at a rate of 5–50 cm/1000 years, leading to a small to moderate (on the order of <~5 °C) temperature effect especially when formation occurs >30–50 cm[41]. Explanation (5) will be discussed below.

Since we consider all the reported data in Table 1 analytically correct (except for one, see above) we calculated soil temperatures from the full dataset, yielding median values of 33.9 and 39.2 °C for the LP and PETM. According to this scenario, the full range of $T_{\Delta47\text{-carb}}$ is considered valid,

Table 1 | Carbon, oxygen and clumped isotope compositions of soil carbonates from mudstone paleosols of the Esplugafreda and Claret Formations, Esplugafreda sequence, Spain

Sample code	Section	Depth (m)	Composite depth (m)	Analysis period	*N*	$\delta^{13}C_{carb}$ [VPDB, ‰]	±1 SD
Yellowish Soils / Claret Formation [PETM body]							
ITS/E-YS1	ITS/east/sec. #4	4.3	39.3	7–16 Jul 2022	14	−11.68	0.13
ITS/E-YS1	ITS/east/sec. #4	4.3	39.3	17–22 Jul 2023	10	−11.64	0.16
ITS/E-YS1_d1	ITS/east/sec. #4	4.3	39.3	2–6 Oct 2023	11	−12.01	0.11
ITS/E-YS1_d2	ITS/east/sec. #4	4.3	39.3	2–6 Oct 2023	12	−12.45	0.12
ITS/E-YS1_d3	ITS/east/sec. #4	4.3	39.3	3–7 Oct 2023	12	−12.63	0.02
ITS/E-YS3	ITS/east/sec. #4	3.7	38.7	3–8 Feb 2023	12	−13.20	0.04
ITS/E-YS5	ITS/east/sec. #4	3.1	38.1	2–19 Jul 2022	15	−10.36	0.14
ITS/E-YS7	ITS/east/sec. #4	2.5	37.5	4–9 Feb 2023	12	−10.12	0.17
ITS/E-YS9	ITS/east/sec. #4	1.9	36.9	1–18 Jul 2022	15	−11.22	0.15
ITS/E-YS9_d1	ITS/east/sec. #4	1.9	36.9	3–7 Oct 2023	12	−13.12	0.13
ITS/E-YS9_d2	ITS/east/sec. #4	1.9	36.9	3–7 Oct 2023	12	−12.49	0.08
ITS/E-YS9_d3	ITS/east/sec. #4	1.9	36.9	3–7 Oct 2023	12	−12.29	0.06
ITS/E-YS13	ITS/east/sec. #4	0.7	35.7	2–19 Jul 2022	15	−12.58	0.17
ITS/E-YS13	ITS/east/sec. #4	0.7	35.7	18–22 Jul 2022	12	−12.53	0.08
ITS/E-YS13	ITS/east/sec. #4	0.7	35.7	29 Aug–3 Sep 2023	11	−12.42	0.05
ITS/W-YS2	ITS/west/sec. #6	16	36	9–16 Jul 2022	15	−11.51	0.11
ITS/W-YS4	ITS/west/sec. #6	14	34	8–16 Jul 2022	15	−12.18	0.06
ITS/W-YS7	ITS/west /sec. #6	11	31	8–16 Jul 2022	17	−12.35	0.06
ITS/W-YS7	ITS/west/sec. #6	11	31	3–8 Feb 2023	12	−13.45	0.03
ITS/W-YS10	ITS/west/sec. #6	8	28	1–18 July 2022	16	−13.84	0.02
ITS/W-YS10	ITS/west/sec. #6	8	28	29 Aug–2 Sep 2023	11	−13.74	0.03
Esplugafreda Formation vertisols [late Paleocene]							
ITS-EF sc 5.3	ITS/east/sec. #5/prof. #1	5.3	61.3	2–19 Jul 2022	12	−6.36	0.06
ITS-EF sc 5.3	ITS/east/sec. #5/prof. #1	5.3	61.3	5–11 May 2023	12	−6.29	0.06
ITS-EF sc 6.6	ITS/east/sec. #5/prof. #1	6.6	62.6	24 Oct–8 Nov 2023	11	−8.55	0.14
ITS-EF sc 26.40	ITS/east/sec. #5/prof. #1	26.4	82.4	12–16 Jul 2022	15	−6.39	0.05
ITS-EF sc 26.40	ITS/east/sec. #5/prof. #1	26.4	82.4	4–10 Feb 2023	12	−6.69	0.07
ITS-EF sc 10.7	ITS/east/sec. #5/prof. #2	10.7	98.7	4–9 Feb 2023	12	−7.43	0.07
ITS-EF sc 19.9	ITS/east/sec. #5/prof. #2	19.9	108.9	2–19 Jul 2022	15	−7.08	0.03
ITS-EF sc 19.9	ITS/east/sec. #5/prof. #2	19.9	108.9	6–11 May 2023	10	−7.02	0.02
ITS-EF sc 19.9	ITS/east/sec. #5/prof. #2	19.9	108.9	24 Oct–8 Nov 2023	11	−7.47	0.10
ITS-EF sc 21.2	ITS/east/sec. #5/prof. #2	21.2	110.2	25 Oct–9 Nov 2023	12	−6.68	0.14
ITS-EF sc 29.2	ITS/east/sec. #5/prof. #3	29.2	118.2	25 Oct–9 Nov 2023	10	−7.32	0.11
ITS-EF sc 35.7	ITS/east/sec. #5/prof. #4	35.7	124.7	25 Oct–9 Nov 2023	8	−6.93	0.13
ITS-EF sc 35.7	ITS/east/sec. #5/prof. #4	35.7	124.7	9–16 Apr 2024	15	−6.98	0.36
ITS-EF sc 36.95	ITS/east/sec. #5/prof. #4	36.95	125.95	25 Oct–9 Nov 2023	8	−6.16	0.07
ITS-EF sc 47.9	ITS/east/sec. #5/prof. #4	47.9	136.9	4–9 Feb 2023	9	−5.85	0.04

$\delta^{18}O_{carb}$ [VPDB, ‰]	±1 SD	$\delta^{18}O_{carb}$ [VSMOW, ‰]	±1 SD	$\Delta_{47\text{-}carb}$ [I-CDES, ‰]	±1SE	±95% CL	$T_{47\text{-}carb}$ [°C][a]	±1SE	±95% CL	$\delta^{18}O_{soil\text{-}w}$ [VSMOW, ‰][b]	±1SD
−5.92	0.06	24.81	0.06	0.534	0.010	0.020	47.6	4.9	8.8	0.72	0.05
−5.91	0.07	24.82	0.07	0.553	0.011	0.022	40.0	5.0	9.1	−0.64	0.06
−6.01	0.04	24.72	0.04	0.562	0.005	0.010	36.3	2.9	4.4	−1.43	0.04
−6.06	0.05	24.67	0.05	0.559	0.008	0.015	37.6	3.7	6.2	−1.23	0.05
−6.08	0.03	24.65	0.03	0.550	0.009	0.018	40.9	4.3	7.6	−0.64	0.05
−6.15	0.05	24.58	0.05	0.564	0.008	0.016	35.6	3.7	6.3	−1.69	0.05
−5.94	0.10	24.80	0.10	0.567	0.007	0.014	34.4	3.4	5.7	−1.70	0.05
−6.11	0.12	24.62	0.12	0.569	0.011	0.021	33.9	4.6	8.2	−1.97	0.07
−5.84	0.06	24.90	0.06	0.546	0.009	0.017	42.6	4.1	7.1	−0.08	0.05
−6.02	0.06	24.71	0.06	0.568	0.006	0.011	34.1	3.0	4.7	−1.84	0.04

Table 1 (continued) | Carbon, oxygen and clumped isotope compositions of soil carbonates from mudstone paleosols of the Esplugafreda and Claret Formations, Esplugafreda sequence, Spain

$\delta^{18}O_{carb}$ [VPDB, ‰]	±1 SD	$\delta^{18}O_{carb}$ [VSMOW, ‰]	±1 SD	$\Delta_{47\text{-carb}}$ [I-CDES, ‰]	±1SE	±95% CL	$T_{47\text{-carb}}$ [°C][a]	±1SE	±95% CL	$\delta^{18}O_{soil\text{-}w}$ [VSMOW, ‰][b]	±1SD
−6.01	0.03	24.73	0.03	0.553	0.009	0.017	39.9	4.1	7.1	−0.74	0.05
−5.99	0.04	24.75	0.04	0.557	0.009	0.018	38.4	4.1	7.2	−1.00	0.05
−6.03	0.12	24.71	0.12	0.510	0.009	0.018	58.2	5.0	8.9	2.42	0.04
−6.14	0.17	24.59	0.17	0.576	0.008	0.016	31.4	3.6	6.0	−2.48	0.06
−5.99	0.08	24.75	0.08	0.550	0.009	0.018	41.1	4.3	7.5	−0.51	0.05
−5.84	0.06	24.90	0.07	0.549	0.007	0.013	41.6	3.5	5.7	−0.27	0.04
−5.95	0.08	24.78	0.08	0.550	0.008	0.015	41.0	3.8	6.4	−0.48	0.05
−6.33	0.11	24.40	0.11	0.610	0.011	0.021	19.8	3.9	6.9	−5.00	0.10
−5.97	0.03	24.76	0.04	0.570	0.007	0.013	33.5	3.2	5.2	−1.91	0.05
−5.84	0.03	24.90	0.03	0.512	0.010	0.019	57.3	5.2	9.3	2.46	0.05
−5.81	0.08	24.94	0.08	0.561	0.012	0.023	36.9	5.0	9.1	−1.10	0.07
−4.54	0.05	26.24	0.05	0.571	0.009	0.017	33.1	3.9	6.7	−0.56	0.06
−4.52	0.07	26.26	0.07	0.569	0.007	0.014	33.9	3.4	5.6	−0.37	0.05
−5.46	0.05	25.30	0.05	0.562	0.012	0.024	36.6	5.2	9.4	−0.81	0.07
−4.47	0.08	26.31	0.08	0.527	0.009	0.018	50.7	4.6	8.0	2.72	0.05
−4.59	0.08	26.19	0.08	0.593	0.009	0.017	25.3	3.6	6.1	−2.14	0.07
−4.95	0.08	25.81	0.09	0.588	0.007	0.016	27.0	3.2	5.3	−2.17	0.06
−4.57	0.08	26.21	0.08	0.564	0.010	0.020	35.7	4.4	7.7	−0.09	0.06
−4.60	0.04	26.18	0.04	0.559	0.005	0.011	37.5	3.0	4.6	0.23	0.04
−4.77	0.06	26.00	0.06	0.596	0.009	0.018	24.4	3.8	6.5	−2.49	0.08
−4.55	0.05	26.23	0.06	0.607	0.014	0.028	20.5	5.0	9.3	−3.08	0.12
−5.44	0.06	25.31	0.07	0.574	0.012	0.023	31.8	4.7	8.5	−1.71	0.07
−5.41	0.04	25.35	0.04	0.517	0.010	0.019	54.9	4.9	8.8	2.50	0.04
−5.54	0.11	25.20	0.12	0.524	0.008	0.016	51.8	4.3	7.3	1.82	0.04
−4.13	0.04	26.67	0.04	0.569	0.008	0.015	33.9	3.6	6.1	0.02	0.05
−4.47	0.04	26.32	0.04	0.585	0.007	0.014	28.0	3.2	5.2	−1.47	0.06

ITS Italian section, *sec.* section, *prof.* profile, *N* number of replicates from the same sample powder, *d1-d3* points of internal transect across the carbonate

[a]Soil carbonate formation temperatures were calculated with the unified Anderson et al.[90] Δ_{47}–T calibration

[b]Oxygen isotope compositions of the soil water (=precipitation) was calculated from the Δ_{47}-based formation temperatures and the calcite-water fractionation factor of Kim and O'Neil[102]

including seemingly anomalous values. Provided that formed close (<20 cm) to the soil surface, some $T_{\Delta47\text{-carb}}$ values exceeding 40 °C may record real T_{soil} due to radiative heating of the ground surface[40,41] under the extreme warm conditions and sparse vegetation[30] of the LP and PETM at Esplugafreda. Based on the above figures, a significant soil temperature warming on the order of ~5 °C is obtained for the PETM, provided that there was no significant seasonal shift in SC formation between the LP and PETM intervals.

Comparison of proxy-based and simulated temperatures: implications for PETM warming and latitudinal temperature gradients

Simultaneous air and ground surface temperature measurements demonstrate a strong coupling between these two climatic parameters under modern climatic conditions[65]. The temperature difference between the two variables was found to be 2.47 K on average, exhibiting a seasonal variation with ~1–4 K difference over the winter and summer seasons due to changing incident solar radiation[66]. Subsequent studies concluded that soil radiative heating is limited, <2 K for clayey soils[67] and <3 °C for most soils below 50 cm[68]. In another study, Molnar[69] established relationships between T_{soil} and MAT (ΔT_{soil}–MAT) for various land surface covers on theoretical grounds and using FLUXNET2015 datasets. Dependent on surface wetness/aridity, ΔT_{soil}–MAT was found to be between 1 and 4 °C for shrublands and 1–3 °C for grasslands. However, these values are given for the soil surface, while soil nodules do not usually form close to the ground surface (<20–50 cm). Based on this fact and previous evidence for sparse vegetation and prevailing arid/semi-arid climate with seasonal precipitation at the Esplugafreda site over the LP and PETM intervals[30,31], we considered a T_{soil}–air temperature difference of 0–3 °C to put our T_{soil} average values in a paleoclimate modelling context.

Mean summer air temperatures at the Esplugafreda site must have been around 30.9–33.9 °C over the LP, calculating with the median $T_{\Delta47\text{-carb}}$ value and subtracting 0–3 °C as discussed above. In comparison with DeepMIP model ensembles of near-surface air temperatures (Fig. 5), these values agree well with the summer season temperatures (T_{JJA}) of the DeepMIP × 2 simulation for a CO_2 concentration of 560 ppm and is slightly lower than those of DeepMIP × 3 (840 ppm), which is closer to the 900 ± 100 ppm CO_2 estimate for the pre-PETM interval[70]. For the PETM, the mean summer air temperature is estimated to be 36.2–39.2 °C (same approach), in good correspondence with both the DeepMIP ×4 and ×6 (1120 and 1680 ppm) simulation results for the summer season. As such, this provides evidence for a summer season bias for SC growth, which would be expected considering the warm temperatures and excessive evaporation and drying (potentially after larger precipitation infiltration events[44]; Fig. 5b) during the June to August period simulated for the study region in front of the Pyrenees[71]. Since the mean soil and air temperatures obtained from both SC populations of LP and PETM age seem to reflect summer season temperatures, it is less likely that the temperature differences reconstructed between the LP and PETM intervals at Esplugafreda would have been caused by a significant seasonal shift in carbonate formation. Thus, the

~+5 °C mean warm-season anomaly between the LP and PETM found at Esplugafreda is regarded as a robust estimate, which matches well the simulated range of 4–6 °C of mean summer temperature warming in this region[26,71]. A recent study has reconstructed a slightly smaller warming of ~3 °C between the POE (24.2 ± 1.0 °C) and the PETM (27.0 ± 0.8 °C) using the hydrogen and oxygen isotope compositions of smectites[72]. However, this is not an estimate for the summer season, rather, it represents the difference in MATs. In order to make a comparison of the PETM temperature values reconstructed by the two different methods, we use the MAT-T_{JJA} relationship calculated from the DeepMIP models (see Supplementary Fig. 13). The smectite-based MAT of 27.0 ± 0.8 °C reconstructed by Jaimes-Gutierrez et al.[72] yields a T_{JJA} value of 34.8 ± 3.7 °C, which statistically overlaps with the mean T_{JJA} range of 36.2–39.2 °C calculated from soil carbonates in this study.

The available continental temperature proxy data indicate that the late Palaeocene, and in particular the PETM, was not only a period of significantly higher temperatures than the present day, but that the climate at the Palaeocene-Eocene boundary was characterised by a more even distribution of heat across latitudes than at present[21]. The latest Eocene DeepMIP climate models clearly demonstrate this reduced meridional surface temperature gradient[22,46,73], showing relatively good agreement with the continental proxy data (Fig. 6). In particular, models run for CO_2 levels typical of the LP and early Eocene demonstrate a significantly reduced temperature gradient (0.4–0.5 °C/deg.) for the region between 50 and 75°N latitudes. However, the proxy data suggest an even smaller continental thermal gradient, closer to the latest estimate (~0.3 °C/deg.)[23].

Methods

Depositional setting, stratigraphy and sampling

The Tremp-Graus Basin developed as a piggy-back basin during the early Paleogene[74], which was located at ~32.3°N paleolatitude and preserves terrestrial clastic deposits, informally named "Garumnian" (formally: Tremp Group) and composed of the Thanetian to early Ypresian age Esplugafreda and Claret Formations[28,75]. These continental deposits interfinger to the west with lacustrine and shallow marine carbonates[30] and are under-/overlain by the transitional Aren Sandstone Formation (Maastrichtian) and the shallow marine "Alveolina limestone" (lower Ypresian) (Fig. 1 and Supplementary Fig. 1)[28].

The 165–350 m thick, alluvial EF is made up of cumulative red mudstone paleosols (Fig. 2, Supplementary Figs. 2 and 3) and contains numerous multi-episodic channel-like bodies of calcareous conglomerates and calcarenites (Schmitz and Pujalte, 2007). The paleosols contain abundant centimetre-sized soil nodules and gypsum, and the two pedotypes (Pont d'Orrit and Areny) recognised by Basilici et al.[31] belong to the vertisol order. An erosion surface associated with the incision of a valley network defines the boundary between the Esplugafreda and Claret Formations[28,29].

The 10–70 m thick Claret Formation is composed of a suite of mudstones, sandstones, and conglomerates, with local gypsum accumulations and consists of five members[28]. Member 1 comprises the deposits, mostly grey calcarenites and marlstones to red marls, infilling several incised valleys[30]. Member 2 is a 0.5-7 m thick[30], extensive, sheet-like conglomeratic unit with clasts dominantly in the 20–40 cm range[28], called the Claret Conglomerate (CC) (Supplementary Figs. 2–4). The CC has been suggested to be deposited either by braided rivers[29,63] or an alluvial megafan[15], the latter interpretation implying a dramatic change in the hydrological cycle at the PETM onset. Member 3, the Yellowish Soils (YS), is up to 20 m thick and consists of yellowish silty mudstones with purple mottling (Supplementary Fig. 4) and dispersed, small-sized (0.5–1 cm) carbonate nodules, with intercalated sandstone bodies[28,30]. Member 4, the Gypsum-rich Unit (GrU), is represented by red mudstones with gypsum occurring either as veins, root-like concretions, or centimetre sized nodules[28]. Member 5, the Upper reddish Unit (UrU), which only exists at Esplugafreda, is up to 17 m thick and is made up of red mudstone with dispersed carbonate nodules. The overlying "Alveolina limestone" (AL) is a time-transgressive marine unit, which onlaps member 5 at Esplugafreda[30].

Bulk sediment samples were collected in ~1 m resolution for grain size, mineralogical and organic matter carbon isotope analyses from sections #1–3 and 5 (Supplementary Figs. 1 and 2), representing the Esplugafreda and Claret Formations. A composite profile was created using sections #1, 2 and 5, with the Claret Conglomerate being the reference horizon, while sedimentological and geochemical data from sections #3 and #7 are not discussed in this study. Soil carbonates for clumped isotope analyses were exclusively collected in section #5 (EF) in irregular intervals and sections #4 and #6 (Claret Formation, Member 3: Yellowish Soils) in ~0.3 and ~1 m resolution (Supplementary Fig. 2). Most paleosols of the EF and the yellow soils are cumulative in nature, implying that these soil profiles are generated by slow and continuous sedimentation[32]. This process leads to gradual overprinting as the soil profile aggrades and the paleosol profile boundaries are diffuse and not marked by deposits or erosional surfaces[31]. Consequently, the depth of soil carbonate formation cannot be constrained.

Grain size and mineralogical analyses

Prior to laser diffraction measurements, samples (~3 g) were pretreated with 10 ml 20% H_2O_2 and 10 ml 10% HCl to remove organic matter and carbonates. Subsequently, samples were mixed with 10 ml of 0.05 N $Na(PO_3)_6$, and ultrasonicated for about 1 min. Grain size of bulk sediment samples was analysed using a Malvern Mastersizer 3000 laser diffractometer at the Szentágothai Research Centre (SRC), University of Pécs. This instrument has a measurement range of 0.01–3500 µm, divided into 100 size bins. Constants of 1.33 for the refractive index of water, 1.544 for the refractive index of solid phases, and an absorption index of 0.1 were applied. Bulk grain size analyses reported in this study are the averages of three successive laser diffraction runs, and the Malvern Mastersizer 3000 software (version 3.10) was used to transform diffraction data to grain size based on the Mie Scattering Theory. Grain size statistics (mean, median) and the volume percentage values of various grain size fractions were calculated from the Mastersizer 3000 software outputs using the latest 9.1 version of GRADISTAT[76].

Bulk and clay mineralogical analyses were performed at the Institute for Geological and Geochemical Research (IGGR, HUN-REN Research Centre for Astronomy and Earth Sciences, Budapest). The clay fraction (<2 µm) was separated by wet sedimentation after hydrogen peroxide and acetic acid treatments by adding 10% H_2O_2 and 10% CH_3COOH to the samples sequentially until suspension no longer effervesced. The remaining material was then sedimented on glass slides for X-ray diffraction (XRD) analysis following a modified USGS methodology[77]. Samples were subject to ethylene-glycol solvation (at 60 °C, overnight) and heating at 550 °C (1 h) for diagnosing smectite and kaolinite. XRD measurements were performed on a RIGAKU Miniflex 600 equipment at 45 kV voltage and 35 mA current applying a graphite monochromator with CuKα radiation. The 2θ range was set to 2–70° and a counting speed of 0.05°/2 s was applied for the analyses. The Rigaku PDXL2 software was used for phase identification based on the ICDD database. Quantitative analyses of bulk mineralogy were carried out with full profile fitting combined with Rietveld refinement using the SiroQuant V4.0 software. Clay mineral compositions were determined on sedimented samples by semi-quantitative phase analysis following the method of Biscaye[78].

Petrography

Internal structures of half-cut soil carbonates were investigated by a Nikon SMZ 800N stereomicroscope. Cathodoluminescence (CL) analysis of SCs was performed using a Reliotron cold-cathode equipment mounted on a Nikon E600 polarizing microscope. The equipment operated at 5–10 kV accelerating voltage and 0.4–1.2 mA current. CL images were obtained using a defocused electron beam and a Nikon Coolpix 4500 digital camera with automatic exposure.

Organic matter carbon isotope analysis

Bulk sediment samples (~2.5 g each) were powdered and treated with 10% HCl to remove carbonates until the effervescence (CO_2 formation) ceased.

Subsequently, the samples were centrifuged and washed three times in distilled water and dried in an oven at ~60–65 °C. The dried samples were powdered again and 2.5-3 mg aliquots were packed in Sn capsules for stable carbon isotope measurements performed at the IGGR. Samples were combusted using an Organic Elemental Analyzer (Thermo Scientific, Rhodano, Italy) and the yielded gases were transferred via a Conflo III into an isotope ratio mass spectrometer (Delta V Advantage, Thermo Finnigan) operating in continuous flow mode with a carrier gas of He + O_2 and flow speed of 90 ml/min. A two-point linear normalisation was applied to recalculate raw isotope values to the VPDB scale[79] by measuring reference standards IAEA-CH-6 ($\delta^{13}C$: −10.45‰) and IAEA-CH-7 ($\delta^{13}C$: −32.151‰)[80]. Standard deviation of the reference standards were <0.06‰ (IAEA-CH-6, $n = 114$) and <0.05‰ (IAEA-CH-7, $n = 116$) for $\delta^{13}C$. Each unknown sample was measured three times and the average carbon isotope ratios of the bulk organic matter are reported in permil (‰) using the δ-notation.

Soil carbonate carbon, oxygen and clumped isotope analyses

Stable carbon, oxygen and clumped isotope analyses of soil carbonates were performed at the HUN-REN Institute for Nuclear Research (ATOMKI), on a Thermo Scientific™ 253 Plus 10 kV high-resolution Isotope Ratio Mass Spectrometer following phosphoric acid digestion at 70 °C using a Thermo Scientific Kiel IV automatic carbonate device, which is coupled by inert silica coated capillary to the IRMS. For the digestion, 3 drops of 1.95 g/cm^3 phosphoric acid were applied on each carbonate sample. An additional Thermo Scientific™ PoraPak Unit is installed between the two cold fingers of the Kiel IV device, the first one being a water trap and cold finger whereas the second one is a preparation cold finger. The role of the PoraPak column is to decrease organic contamination of the extracted CO_2 gas. This column is filled with PoraPak™ Q 50–80 mesh porous polymer adsorbent and sealed with glass wool at both ends. The trap operation temperature is –30 °C and an hour long regeneration process is done at 120 °C following the measurement of a full sample magazine. After cryogenic purification the CO_2 gas is measured against a working CO_2 gas (Linde AG, $\delta^{13}C_{V\text{-}PDB} = -3.9$ ‰, $\delta^{18}O_{V\text{-}PDB} = -12.5$ ‰, purity = 99.998%) for m/z 44-49 in micro-volume inlet mode and following the long integration dual inlet (LIDI) method[81,82].

Aliquots of 100–140 µg of each unknown sample, collected using a dental drill from the visually most homogeneous, micritic parts of the soil carbonates, were replicated 8–16 times (12 on average) and measured alongside carbonate standards (100–110 µg). For some carbonates a second/third aliquot was also used representing a different sub-sample of the sample powder from the same drilling. For two carbonates (ITS/E-YS1 and YS9), numerous independent samples were drilled at several points across the carbonate interior (labelled d1-d3 in Table 1), and thus these aliquots represent different domains of the same soil carbonate.

The pressure-sensitive baseline (PBL) correction method of Bernasconi et al.[83] was applied to correct the raw beam signals for negative background caused by secondary electrons on higher Faraday-cup detectors. The PBL correction algorithm, which is implemented in the Easotope software (Release 20190125)[84], used peak scans at four different intensities. Our methodology followed the full carbonate-based standardisation scheme[85] using the ETH-1, ETH-2, and ETH-3 InterCarb calcite standards[86]. Consequently, Δ_{47} values are presented on the I-CDES scale (Intercarb-Carbon Dioxide Equilibrium Scale)[86]. Corrections for ion-source non-linearity effects were done using measured ETH-1 and ETH-2 values, while the transfer function to I-CDES was determined using ETH-1, ETH-2, and ETH-3. IAEA-C2 was used as a monitoring sample to determine long-term reproducibility, which was found to be between 0.030 and 0.032‰ (1 SD) during the measurement periods. The 1 SD uncertainties of ETH-1, 2 and 3 carbonate standards ranged between 0.029–0.032‰, 0.028–0.032‰ and 0.029–0.031‰. Alongside the clumped isotope analyses, the conventional carbonate stable isotope compositions of the studied samples were also determined using ETH-1, ETH-2 and ETH-3 as normalisation standards[87]. The applied $\delta^{18}O$ (70 °C) acid fractionation factor for calcite was 1.008709043[88].

Data evaluation, standardisation, and analytical error propagations of clumped isotope measurements were performed following the CO_2 Clumped ETH PBL replicate analysis method using the revised IUPAC parameters for ^{17}O correction[89]. Soil carbonate calcification temperatures in °C were calculated using the Δ_{47}-temperature calibration of Anderson et al.[90]. The temperature uncertainties were propagated from the 95% CL of the Δ_{47} value and the uncertainties of the calibration equation.

Paleoclimate simulation data

For a qualitative comparison of the soil carbonate Δ_{47}-based temperatures with paleoclimate model outputs, paleotemperature and precipitation data were obtained from standardised simulations of the early Eocene climate, carried out in the framework of the DeepMIP[46]. Simulation data used represent ensemble means of eight Earth system models run for different atmospheric CO_2 concentrations (DeepMIP 1×-4 and 6×: 280, 560, 840, 1120 and 1680 ppm), plus an associated preindustrial control simulation (piControl: 280 ppm CO_2). Model data were specifically extracted for the paleolatitude of the Esplugafreda site using the DeepMIP online interface at https://data.deepmip.org/[91]. For the calculation of simulated continental heat distribution and meridional (latitudinal) thermal gradients, 2 m air temperature data of all available model runs for each scenario were considered. Note that the number of simulations varies for the different scenarios[46]. All simulations were bilinearly interpolated onto a common grid with 3.75° longitude × 2.5° latitude to compute an ensemble mean for each scenario. Then, the zonal mean and standard deviation of the ensemble mean continental temperature were calculated.

Proxy data of LP and PETM continental paleotemperatures of the northern hemisphere are from published literature including leaf physiognomic data[23,92,93], the MBT′/CBT organic mineral soil temperature proxy[25,94–96] and lignite brGDGT data[97], as well as mammal $\delta^{18}O$[98], smectite $\delta^{18}O$ and δ^2H[72], and soil carbonate clumped isotope data[24,99]. The primary criteria for selecting proxy data were that it should be chronologically well-defined for the LP or PETM period and indicative of MAT or T_{JJA}. Paleolatitude of each proxy site was calculated using paleolatitude.org[100] with the Vaes et al.[101] paleomagnetic reference frame.

Data availability

All data reported in this paper are available in the Zenodo repository at https://zenodo.org/records/15629019. Paleoclimate model data in the framework of DeepMIP is freely available via the CEDA data archive[91] (https://archive.ceda.ac.uk/about/).

Received: 22 November 2024; Accepted: 12 June 2025;
Published online: 01 July 2025

References

1. McInerney, F. A. & Wing, S. L. The Paleocene-Eocene Thermal Maximum: a perturbation of carbon cycle, climate, and biosphere with implications for the future. *Annu. Rev. Earth Planet. Sci.* **39**, 489–516 (2011).
2. Zeebe, R. E. & Lourens, L. J. Solar System chaos and the Paleocene–Eocene boundary age constrained by geology and astronomy. *Science* **365**, 926–929 (2019).
3. Tripati, A. & Elderfield, H. Deep-sea temperature and circulation changes at the Paleocene–Eocene thermal maximum. *Science* **308**, 1894–1898 (2005).
4. Sluijs, A. et al. Subtropical Arctic Ocean temperatures during the Palaeocene/Eocene thermal maximum. *Nature* **441**, 610–613 (2006).
5. Dunkley-Jones, T. et al. Climate model and proxy data constraints on ocean warming across the Paleocene–Eocene Thermal Maximum. *Earth Sci. Rev.* **125**, 123–145 (2013).
6. Piedrahita, V. A. et al. Orbital phasing of the Paleocene-Eocene Thermal Maximum. *Earth Planet. Sci. Lett.* **598**, 117839 (2022).
7. Turner, S. K. Constraints on the onset duration of the Paleocene–Eocene Thermal Maximum. *Phil. Trans. R. Soc. A* **376**, 20170082 (2018).

8. Zachos, J. C., Dickens, G. R. & Zeebe, R. E. An early Cenozoic perspective on greenhouse warming and carbon-cycle dynamics. *Nature* **451**, 279–283 (2008).
9. Zeebe, R. E., Zachos, J. C. & Dickens, G. R. Carbon dioxide forcing alone insufficient to explain Palaeocene–Eocene Thermal Maximum warming. *Nat. Geosci.* **2**, 576–580 (2009).
10. Bowen, G. J. et al. Two massive, rapid releases of carbon during the onset of the Palaeocene–Eocene thermal maximum. *Nat. Geosci.* **8**, 44–47 (2015).
11. Storey, M., Duncan, R. A. & Swisher, C. C. Paleocene–Eocene Thermal Maximum and the opening of the Northeast Atlantic. *Science* **316**, 587–589 (2007).
12. Saunders, A. D. Two LIPs and two Earth-system crises: the impact of the North Atlantic Igneous Province and the Siberian Traps on the Earth-surface carbon cycle. *Geol. Mag.* **153**, 201–222 (2016).
13. Gutjahr, M. et al. Very large release of mostly volcanic carbon during the Palaeocene–Eocene Thermal Maximum. *Nature* **548**, 573–577 (2017).
14. Kender, S. et al. Paleocene/Eocene carbon feedbacks triggered by volcanic activity. *Nat. Commun.* **12**, 1–10 (2021).
15. Schmitz, B. & Pujalte, V. Abrupt increase in seasonal extreme precipitation at the Paleocene-Eocene boundary. *Geology* **35**, 215–218 (2007).
16. Carmichael, M. J., Pancost, R. D. & Lunt, D. J. Changes in the occurrence of extreme precipitation events at the Paleocene–Eocene thermal maximum. *Earth Planet. Sci. Lett.* **501**, 24–36 (2018).
17. Rush, W. D., Kiehl, J. T., Shields, C. A. & Zachos, J. C. Increased frequency of extreme precipitation events in the North Atlantic during the PETM: observations and theory. *Palaeogeogr. Palaeoclimatol. Palaeoecol.* **568**, 110289 (2021).
18. Ravizza, G., Norris, R. N., Blusztajn, J. & Aubry, M.-P. An osmium isotope excursion associated with the late Paleocene Thermal Maximum: evidence of intensified chemical weathering. *Paleoceanography* **16**, 155–163 (2001).
19. Pogge von Strandmann, P. A. E. et al. Lithium isotope evidence for enhanced weathering and erosion during the Paleocene-Eocene Thermal Maximum. *Sci. Adv.* **7**, eabh4224 (2021).
20. Evans, D. et al. Eocene greenhouse climate revealed by coupled clumped isotope-Mg/Ca thermometry. *Proc. Natl. Acad. Sci. USA* **115**, 1174–1179 (2018).
21. Greenwood, D. R. & Wing, S. L. Eocene continental climates and latitudinal temperature gradients. *Geology* **23**, 1044–1048 (1995).
22. Huber, M. & Caballero, R. The early Eocene equable climate problem revisited. *Clim. Past* **7**, 603–633 (2011).
23. van Dijk, J. et al. Spatial pattern of super-greenhouse warmth controlled by elevated specific humidity. *Nat. Geosci.* **13**, 739–744 (2020).
24. Snell, K. E. et al. Hot summers in the Bighorn Basin during the early Paleogene. *Geology* **41**, 55–58 (2013).
25. Naafs, B. D. A. et al. High temperatures in the terrestrial mid-latitudes during the early Palaeogene. *Nat. Geosci.* **11**, 766–771 (2018).
26. Tierney, J. et al. Spatial patterns of climate change across the Paleocene–Eocene Thermal Maximum. *Proc. Natl. Acad. Sci. USA* **119**, e2205326119 (2022).
27. Schmitz, B. & Pujalte, V. Sea-level, humidity, and land-erosion records across the initial Eocene thermal maximum from a continental-marine transect in northern Spain. *Geology* **31**, 689–692 (2003).
28. Pujalte, V., Schmitz, B. & Baceta, J. I. Sea-level changes across the Paleocene–Eocene interval in the Spanish Pyrenees, and their possible relationship with North Atlantic magmatism. *Palaeogeogr. Palaeoclimatol. Palaeoecol.* **393**, 45–60 (2014).
29. Colombera, L., Arévalo, O. J. & Mountney, N. P. Fluvial-system response to climate change: the Paleocene-Eocene Tremp Group, Pyrenees, Spain. *Global Planet. Change* **157**, 1–17 (2017).
30. Payros, A., Pujalte, V. & Schmitz, B. Mid-latitude alluvial and hydroclimatic changes during the Paleocene–Eocene Thermal Maximum as recorded in the Tremp-Graus Basin, Spain. *Sediment. Geol.* **435**, 106155 (2022).
31. Basilici, G. et al. Variations from dry to aquic conditions in Vertisols (Esplugafreda Formation, Eastern Pyrenees, Spain): implications for late Paleocene climate change. *Palaeogeogr. Palaeoclimatol. Palaeoecol.* **595**, 110972 (2022).
32. Wright, V. P. & Marriott, S. B. A quantitative approach to soil occurrence in alluvial deposits and its application to the Old Red Sandstone of Britain. *J. Geol. Soc. London* **153**, 907–913 (1996).
33. Tremblin, M. et al. Mercury enrichments of the Pyrenean foreland basins sediments support enhanced volcanism during the Paleocene-Eocene thermal maximum (PETM). *Glob. Planet. Change* **212**, 103794 (2022).
34. Korasidis, V. A., Wing, S. L., Shields, C. A. & Kiehl, J. T. Global changes in terrestrial vegetation and continental climate during the Paleocene-Eocene Thermal Maximum. *Paleoceanogr. Paleoclimatol.* **37**, e2021PA004325 (2022).
35. Ghosh, P. et al. ^{13}C–^{18}O bonds in carbonate minerals: a new kind of paleothermometer. *Geochim. Cosmochim. Acta* **70**, 1439–1456 (2006).
36. Eiler, J. M. Paleoclimate reconstructions using carbonate clumped isotope thermometry. *Quat. Sci. Rev.* **30**, 3575–3588 (2011).
37. Cerling, T. E. & Quade, J. Stable carbon and oxygen isotopes in soil carbonates. In *Climate Change in Continental Isotopic Records* Vol. 78 (eds Swart, P.K., Lohmann, K.C., McKenzie, J. & Savin, S.) 217–231 (AGU, 1993).
38. Breecker, D. O., Sharp, Z. D. & McFadden, L. D. Seasonal bias in the formation and stable isotopic composition of pedogenic carbonate in modern soils from Central New Mexico, USA. *Geol. Soc. Am. Bull.* **121**, 630–640 (2009).
39. Cerling, T. E. The stable isotopic composition of modern soil carbonate and its relationship to climate. *Earth Planet. Sci. Lett.* **71**, 229–240 (1984).
40. Passey, B. H., Levin, N. E., Cerling, T. E., Brown, F. H. & Eiler, J. M. High-temperature environments of human evolution in East Africa based on bond ordering in paleosol carbonates. *Proc. Natl. Acad. Sci. USA* **107**, 11245–11249 (2010).
41. Quade, J., Eiler, J., Daëron, M. & Achyuthan, H. The clumped isotope geothermometer in soil and paleosol carbonate. *Geochim. Cosmochim. Acta* **105**, 92–107 (2013).
42. Peters, N. A., Huntington, K. W. & Hoke, G. D. Hot or not? Impact of seasonally variable soil carbonate formation on paleotemperature and O-isotope records from clumped isotope thermometry. *Earth Planet. Sci. Lett.* **361**, 208–218 (2013).
43. Hough, B. G., Fan, M. & Passey, B. H. Calibration of the clumped isotope geothermometer in soil carbonate in Wyoming and Nebraska, USA: implications for paleoelevation and paleoclimate reconstruction. *Earth Planet. Sci. Lett.* **391**, 110–120 (2014).
44. Burgener, L. et al. Variations in soil carbonate formation and seasonal bias over>4 km of relief in the western Andes (30°S) revealed by clumped isotope thermometry. *Earth Planet. Sci. Lett.* **441**, 188–199 (2016).
45. Breecker, D. O. et al. CO_2 concentrations in vertisols: seasonal variability and shrink-swell. In *New Frontiers in Paleopedology and Terrestrial Paleoclimatology: Paleosols and Soil Surface Analog Systems* Vol. 104 (eds Driese, S.G., Nordt, L.C. & McCarthy, P.J.) 35–45 (SEPM Special Publications, 2013).
46. Lunt, D. J. et al. DeepMIP: model intercomparison of early Eocene climatic optimum (EECO) large-scale climate features and comparison with proxy data. *Clim. Past* **17**, 203–227 (2021).
47. Wright, V. P. A micromorphological classification of fossil and recent calcic and petrocalcic microstructures. In *Soil Micromorphology: A*

Basic and Applied Science (ed. Douglas, L.A.) 401–407 (Elsevier, 1990).
48. Pimentel, N. L., Wright, V. P. & Azevedo, T. M. Distinguishing early groundwater alteration effects from pedogenesis in ancient alluvial basins: examples from the Palaeogene of southern Portugal. *Sed. Geol.* **105**, 1–10 (1996).
49. Mack, G. H., Cole, D. R. & Trevino, L. The distribution and discrimination of shallow, authigenic carbonate in the Pliocene–Pleistocene Palomas Basin, southern Rio Grande rift. *Geol. Soc. Am. Bull.* **112**, 643–656 (2000).
50. Hemming, N. G., Meyers, W. J. & Grams, J. C. Cathodoluminescence in diagenetic calcites: the roles of Fe and Mn as deduced from electron probe and spectrophotometric measurements. *J. Sediment. Petrol.* **59**, 404–411 (1989).
51. Mintz, J. S., Driese, S. G., Breecker, D. O. & Ludvigson, G. A. Influence of changing hydrology on pedogenic calcite precipitation in Vertisols, Dance Bayou, Brazoria County, Texas, USA: implications for estimating paleoatmospheric pCO_2. *J. Sediment. Res.* **81**, 394–400 (2011).
52. Kraus, M. J. & Hasiotis, S. T. Significance of different modes of rhizolith preservation to interpreting palaeoenvironmental and palaeohydrologic settings: examples from Palaeogene palaeosols, Bighorn Basin, Wyoming, U.S.A. *J. Sediment. Res.* **76**, 633–646 (2006).
53. Kelson, J. R. et al. A proxy for all seasons? A synthesis of clumped isotope data from Holocene soil carbonates. *Quat. Sci. Rev.* **234**, 106259 (2020).
54. Havranek, R., Snell, K., Brookins, S. & Davidheiser-Kroll, B. Timing of pedogenic carbonate formation in fine-grained soils: decoupled $T(\Delta_{47})$ and $\delta^{18}O_w$ seasonal bias. *Paleoceanogr. Paleoclimatol.* **40**, e2024PA005071 (2025).
55. Manners, H. R. et al. Magnitude and profile of organic carbon isotope records from the Paleocene–Eocene Thermal Maximum: evidence from northern Spain. *Earth Planet. Sci. Lett.* **376**, 220–230 (2013).
56. Gallagher, T. M., Cacciatore, C. G. & Breecker, D. O. Interpreting the difference in magnitudes of PETM carbon isotope excursions in paleosol carbonate and organic matter: oxidation of methane in soils versus elevated soil respiration rates. *Paleoceanogr. Paleoclimatol.* **34**, 2113–2128 (2019).
57. Zhu, J. et al. Simulation of early Eocene water isotopes using an Earth system model and its implication for past climate reconstruction. *Earth Planet. Sci. Lett.* **537**, 116164 (2020).
58. Eiler, J. M. & Schauble, E. $^{18}O^{13}C^{16}O$ in Earth's atmosphere. *Geochim. Cosmochim. Acta* **68**, 4767–4777 (2004).
59. Huntington, K. W. et al. Methods and limitations of ' clumped' CO_2 isotope (Δ_{47}) analysis by gas-source isotope ratio mass spectrometry. *J. Mass Spectrom.* **44**, 1318–1329 (2009).
60. Bergmann, K. D. et al. A paired apatite and calcite clumped isotope thermometry approach to estimating Cambro-Ordovician seawater temperatures. *Geochim. Cosmochim. Acta* **224**, 18–41 (2018).
61. Fiebig, J. et al. Carbonate clumped isotope values compromised by nitrate-derived NO_2 interferent. *Chem. Geol.* **670**, 122382 (2024).
62. Tripati, A. K. et al. Beyond temperature: clumped isotope signatures in dissolved inorganic carbon species and the influence of solution chemistry on carbonate mineral composition. *Geochim. Cosmochim. Acta* **166**, 344–371 (2015).
63. Burgener, L. K. et al. Clumped isotope constraints on equilibrium carbonate formation and kinetic isotope effects in freezing soils. *Geochem. Cosmochim. Acta* **235**, 402–430 (2018).
64. Guo W. *Carbonate Clumped Isotope Thermometry: Application to Carbonaceous Chondrites and Effects of Kinetic Isotope Fractionation*. Phd thesis, California Institute of Technology (2009).
65. Melo-Aguilar, C. et al. Near-surface soil thermal regime and land–air temperature coupling: a case study over Spain. *Int. J. Climatol.* **42**, 7516–7534 (2021).
66. Bartlett, M. G., Chapman, D. S. & Harris, R. N. A decade of ground-air temperature tracking at Emigrant Pass Observatory, Utah. *J. Clim.* **19**, 3722–3731 (2006).
67. Cermak, V., Bodri, L., Kresl, M., Dedecek, P. & Safanda, J. Eleven years of ground–air temperature tracking over different land cover types. *Int. J. Climatol.* **37**, 1084–1099 (2016).
68. Burgener, L. K., Hyland, E. G., Huntington, K. W., Kelson, J. R. & Sewall, J. O. Revisiting the equable climate problem during the Late Cretaceous greenhouse using paleosol carbonate clumped isotope temperatures from the Campanian of the Western Interior Basin, USA. *Palaeogeogr. Palaeoclimatol. Palaeoecol.* **516**, 244–267 (2019).
69. Molnar, P. Differences between soil and air temperatures: implications for geological reconstructions of past climate. *Geosphere* **18**, 800–824 (2022).
70. Anagnostou, E. et al. Proxy evidence for state-dependence of climate sensitivity in the Eocene greenhouse. *Nat. Commun.* **11**, 4436 (2020).
71. Kiehl, J. T., Shields, C. A., Snyder, M. A., Zachos, J. C. & Rothstein, M. Greenhouse and orbital-forced climate extremes during the early Eocene. *Philos. Trans. R. Soc. A* **376**, 20170085 (2018).
72. Jaimes-Gutierrez, R. et al. Deciphering Paleocene-Eocene Thermal Maximum climatic dynamics: insights from oxygen and hydrogen isotopes in clay minerals of Paleosols from the Southern Pyrenees. *Paleoceanogr. Paleoclimatol.* **39**, e2024PA004858 (2024).
73. Lunt, D. J. et al. A model–data comparison for a multi-model ensemble of early Eocene atmosphere–ocean simulations: EoMIP. *Clim. Past* **8**, 1717–1736 (2012).
74. Chanvry, E. et al. The influence of intrabasinal tectonics in the stratigraphic evolution of piggyback basin fills: towards a model from the Tremp-Graus-Ainsa Basin (South-Pyrenean Zone, Spain). *Sediment. Geol.* **377**, 34–62 (2018).
75. Dreyer, T. Quantified fluvial architecture in ephemeral stream deposits of the Esplugafreda Formation (Paleocene), Tremp-Graus Basin, northern Spain. In *Alluvial Sedimentation* Vol. 17 (eds Marzo, M. & Puigdefábregas, C.) 337–362 (IAS Special Publication, 1993).
76. Blott, S. J. & Pye, K. GRADISTAT: a grain size distribution and statistics package for the analysis of unconsolidated sediments. *Earth Surf. Process. Landf.* **26**, 1237–1248 (2001).
77. Poppe, L. J., Paskevich, V. F., Hathaway, J. C. & Blackwood, D. S. A laboratory manual for X-ray powder diffraction. Open-File Report 2001-41, USGS (2001).
78. Biscaye, P. E. Mineralogy and sedimentation of recent deep-sea clay in the Atlantic Ocean and adjacent seas and oceans. *Geol. Soc. Am. Bull.* **76**, 803–832 (1965).
79. Paul, D., Skrzypek, G. & Fórizs, I. Normalization of measured stable isotope composition to isotope reference scale – a review. *Rapid Commun. Mass Spectrom.* **21**, 3006–3014 (2007).
80. Coplen, T. B. et al. New guidelines for $\delta^{13}C$ measurements. *Anal. Chem.* **78**, 2439–2441 (2006).
81. Hu, B. et al. A modified procedure for gas-source isotope ratio mass spectrometry: the long-integration dual-inlet (LIDI) methodology and implications for clumped isotope measurements. *Rapid Commun. Mass Spectrom.* **28**, 1413–1425 (2014).
82. Müller, I. et al. Carbonate clumped isotope analyses with the long-integration dual-inlet (LIDI) workflow: scratching at the lower sample weight boundaries. *Rapid Commun. Mass Spectrom* **31**, 1057–1066 (2017).
83. Bernasconi, S. M. et al. Background effects on Faraday collectors in gas source mass spectrometry and implications for clumped isotope measurements. *Rapid Commun. Mass Spectrom.* **27**, 603–612 (2013).
84. John, C. M. & Bowen, D. Community software for challenging isotope analysis: first applications of 'Easotope' to clumped isotopes. *Rapid Commun. Mass Spectrom.* **30**, 2285–2300 (2016).

85. Meckler, A. N. et. al. Long-term performance of the Kiel carbonate device with a new correction scheme for clumped isotope measurement. *Rapid Commun. Mass Spectrom.* **28**, 1705–1725 (2014).
86. Bernasconi, S. M. et al. InterCarb: a community effort to improve inter-laboratory standardization of the carbonate clumped isotope thermometer using carbonate standards. *Geochem. Geophys. Geosyst.* **22**, e2020GC009588 (2021).
87. Bernasconi, S. M. et al. Reducing uncertainties in carbonate clumped isotope analysis through consistent carbonate-based standardization. *Geochem. Geophys. Geosyst.* **19**, 2895–2914 (2018).
88. Kim, S.-T., Coplen, T. B. & Horita, J. Normalization of stable isotope data for carbonate minerals: implementation of IUPAC guideline. *Geochim. Cosmochim. Acta* **158**, 276–289 (2015).
89. Schauer, A. J., Kelson, J., Saenger, C. & Huntington, K. W. Choice of ^{17}O correction affects clumped isotope (Δ_{47}) values of CO_2 measured with mass spectrometry. *Rapid Commun. Mass Spectrom.* **30**, 2607–2616 (2016).
90. Anderson, N. T. et al. A unified clumped isotope thermometer calibration (0.5–1100 °C) using carbonate-based standardization. *Geophys. Res. Lett.* **48**, e2020GL092069 (2021).
91. Steinig, S. et al. Deep-Time Model Intercomparison Project (DeepMIP) Eocene model data version 1.0. NERC EDS Centre for Environmental Data Analysis, https://doi.org/10.5285/95aa41439d564756950f89921b6ef215 (2024).
92. Kowalski, E. A. & Dilcher, D. L. Warmer paleotemperatures for terrestrial ecosystems. *Proc. Natl. Acad. Sci. USA* **100**, 167–170 (2003).
93. Sunderlin, D. et al. Paleoenvironment and paleoecology of a Late Paleocene high-latitude terrestrial succession, Arkose Ridge Formation at Box Canyon, Southern Talkeetna Mountains, Alaska. *Palaeogeogr. Palaeoclimatol. Palaeoecol.* **401**, 57–80 (2014).
94. Weijers, J. W., Schouten, S., Sluijs, A., Brinkhuis, H. & Damsté, J. S. S. Warm arctic continents during the Palaeocene–Eocene thermal maximum. *Earth Planet. Sci. Lett.* **261**, 230–238 (2007).
95. Sluijs, A. et al. Warming, euxinia and sea level rise during the Paleocene–Eocene Thermal Maximum on the Gulf Coastal Plain: implications for ocean oxygenation and nutrient cycling. *Clim. Past* **10**, 1421–1439 (2014).
96. Schoon, P. L., Heilmann-Clausen, C., Schultz, B. P., Sinninghe Damsté, J. S. & Schouten, S. Warming and environmental changes in the eastern North Sea Basin during the Palaeocene–Eocene Thermal Maximum as revealed by biomarker lipids. *Org. Geochem.* **78**, 79–88 (2015).
97. Collinson, M. E. et al. Palynological evidence of vegetation dynamics in response to palaeoenvironmental change across the onset of the Paleocene-Eocene Thermal Maximum at Cobham, Southern England. *Grana* **48**, 38–66 (2009).
98. Fricke, H. C. & Wing, S. L. Oxygen isotope and paleobotanical estimates of temperature and δ18O-latitude gradients over North America during the Early Eocene. *Am. J. Sci.* **304**, 612–635 (2004).
99. Kelson, J. R. et al. Warm terrestrial subtropics during the Paleocene and Eocene: carbonate clumped isotope (Δ_{47}) evidence from the Tornillo Basin, Texas (USA). *Paleoceanogr. Paleoclimatol.* **33**, 1230–1249 (2018).
100. van Hinsbergen, D. J. J. et al. A paleolatitude calculator for Paleoclimate studies. *PLoS ONE* **10**, e0126946 (2015).
101. Vaes, B. et al. A global apparent polar wander path for the last 320 Ma calculated from site-level paleomagnetic data. *Earth Sci. Rev.* **245**, 104547 (2023).
102. Kim, S.-T. & O'Neil, J. R. Equilibrium and nonequilibrium oxygen isotope effects in synthetic carbonates. *Geochim. Cosmochim. Acta* **61**, 3461–3475 (1997).

Acknowledgements

This work was supported by the Hungarian National Research, Development and Innovation Office (NKFIH) through the K-137767 OTKA project. A.P. received funding from the State Research Agency of the Ministry of Science, Innovation and Universities, Spain (PID2019-105670GB-I00/AEI/10.13039/501100011033, Agencia Estatal de Investigación, Ministerio de Ciencia, Innovación y Universidades). K.H.S. thanks the AXA Research Fund for support. Sampling permissions were not required. Insightful and constructive comments of the three anonymous reviewers improved the paper substantially and are much appreciated.

Author contributions

G. Újvári devised the project, performed data analysis and wrote the manuscript. S. Kele helped with funding acquisition and contributed to data analysis. L. Rinyu performed the clumped isotope measurements and verified the datasets. A. Payros provided help with field work and sampling, and together with V. Pujalte and B. Schmitz contributed to geological interpretations; V. Pujalte, B. Schmitz and S.M. Bernasconi supervised the project. Kim H. Stadelmaier did the post-processing of DeepMIP model outputs. J. Kovács conducted grain size analyses, I. Kovács did XRD measurements and B. Bajnóczi performed CL imaging. All authors discussed the results and contributed to the final manuscript.

Funding

Open access funding provided by HUN-REN Research Centre for Astronomy and Earth Sciences.

Competing interests

The authors declare no competing interests.

Additional information

Supplementary information The online version contains supplementary material available at https://doi.org/10.1038/s43247-025-02479-8.

Correspondence and requests for materials should be addressed to Gábor. Újvári.

Peer review information *Communications Earth and Environment* thanks the anonymous reviewers for their contribution to the peer review of this work. Primary Handling Editors: Feifei Zhang, Carolina Ortiz Guerrero and Aliénor Lavergne. [A peer review file is available].